This is the Accepted Manuscript version of an article accepted for publication in Superconductor Science and Technology. IOP Publishing Ltd is not responsible for any errors or omissions in this version of the manuscript or any version derived from it. The Version of Record is available online at DOI: 10.1088/1361-6668/aa980f

An intermetallic powder-in-tube approach to increased flux-pinning in Nb_3Sn by internal oxidation of Zr

L. R. Motowidlo[1], P. J. Lee[2,4,9] , C. Tarantini[2,5], S. Balachandran[2,6], A. K. Ghosh[3,7] and D. C. Larbalestier[2,8]

[1] Deceased, formerly SupraMagnetics Inc, Plantsville, CT 06479, USA
[2] The Applied Superconductivity Center, National High Magnetic Field Laboratory, Florida State University, Tallahassee, FL 32310, USA
[3] Retired, formerly Brookhaven National Laboratory, Upton, NY 11973, USA

E-mail: [4] lee@asc.magnet.fsu.edu, [5] tarantini@asc.magnet.fsu.edu, [6] shreyasb@asc.magnet.fsu.edu, [7] akghosh_11786@yahoo.com, [8] larbalestier@asc.magnet.fsu.edu

Abstract We report on the development of multifilamentary Nb_3Sn superconductors by a versatile powder-in-tube technique (PIT) that demonstrates a simple pathway to a strand with a higher density of flux-pinning sites that has the potential to increase critical current density beyond present levels. The approach uses internal oxidation of Zr-alloyed Nb tubes to produce Zr oxide particles within the Nb_3Sn layer that act as a dispersion of artificial pinning centres (APC). In this design, SnO_2 powder is mixed with Cu_5Sn_4 powder within the PIT core that supplies the Sn for the A15 reaction with Nb1Zr filament tubes. Initial results show an average grain size of ~38 nm in the A15 layer, compared to the 90-130 nm of typical APC-free high-J_c strands made by conventional PIT or Internal Sn processing. There is a shift in the peak of the pinning force curve from H/H_{irr} of ~0.2 to ~0.3 and the pinning force curves can be deconvoluted into grain boundary and point-pinning components, the point-pinning contribution dominating for the APC Nb-1wt%Zr strands.

1. Introduction

Multifilamentary Nb_3Sn strands have a high manufacturing maturity with very large quantities of low hysteresis loss wires produced for the ITER project (600 t) [1] and high current density strands being procured for the High Luminosity (HiLumi) upgrade to the Large Hadron Collider (4.8 t MQXF)[2,3]. For applications that require magnetic fields above 15 T, HTS conductors like Bi-2212 can outperform Nb_3Sn [4] but their cost is still prohibitive for future large scale applications such as the High Energy LHC (HE-LHC) [5] or the Future Circular Collider [6] both of which envision ~16 T dipole operation [7]. However, there are significant challenges to developing Nb_3Sn for practical use in an accelerator at such high fields because the critical current density, J_c, target specification of 2300 A/mm^2 (1.9 K, 16 T) or 1500 A/mm^2 at 16 T, 4.2 K [8] is ~50% higher than that of the present HiLumi procurement [9], which is the highest field and highest J_c accelerator application so far. Improvements in conductor performance are required to provide operating margin, but any performance increase that can lead to a reduction in cost is also highly desirable because the FCC conductor as currently specified is estimated to represent 50% of the magnet cost

[9] Leszek Motowidlo unexpectedly passed away on September 21, 2016, this paper brings together the available data on the powder-in-tube APC Nb_3Sn strand that he had developed. All correspondence should be address to lee@asc.magnet.fsu.edu.

[7]. Although recent developments in the understanding and optimization of Nb_3Sn strand heat treatments have suggested room to improve the critical current density in existing internal Sn [10] and PIT [11] conductors, achieving the FCC specification is a challenge that almost certainly requires enhanced vortex pinning too.

In conventional Nb_3Sn conductors, vortex pinning strength is determined by the grain boundary density [12]. However, a typical grain diameter of ~100 nm is much greater than the ~12 nm fluxoid spacing at 16 T, making the pinning efficiency low. Consequently, there have been a number of attempts to introduce additional pinning sites including the powder metallurgical incorporation of Ta ribbons [13,14], Cu [15,16], Ag [17], and films doped with Ti or Y [18] and Y, Sc, Dy, Al_2O_3, or Ti [19]. However, none of these attempts has been developed into a successful multifilamentary wire. Internal oxidation of Zr-doped Nb was successfully developed for tapes at General Electric (GE) [20]. In the GE tape process, liquid Sn was reacted with Nb foil above 900 °C but the tape critical current density was limited by the resulting large grain size. Doping the Nb tape with Zr and oxygen reduced the A15 grain size to approximately 50 nm (which is ~ half that of modern solid-state reactions). Their TEM studies showed that this process produced coherent ZrO_2 precipitates throughout the Nb_3Sn grains. They also concluded that the slow coarsening of the Nb_3Sn grain size was a result of ZrO_2 precipitates dissolving in shrinking grains and then re-precipitating at the grain boundaries of growing A15 grains. Zeitlin *et al.* [21] attempted to adapt this approach to conventional filamentary internal Sn Nb_3Sn wires by adding SnO_2 to the Sn core of Nb-1wt%Zr (Nb1Zr) filament tubes and they did produce some grain refinement at high temperatures. Further progress was made when Xu *et al*. [22] concluded that the attempts to adapt the GE technique to internal Sn wires had not been successful because the Cu matrix around each filament had less affinity for oxygen than the Sn and thus had prevented oxygen diffusion into the Nb1Zr. Using a Sn-in-Tube architecture Xu *et al*. inserted a SnO_2 layer between the Cu sleeve that normally surrounds the Sn-Cu core and the Nb1Zr matrix and were able to refine the Nb_3Sn grain size to as small as 43 nm. However, scale-up of this approach is challenging because of the required oxide layer between the sleeve and tube. In this paper we demonstrate a potential simplification of this fabrication complexity with a Powder-in-Tube process in which powder mixtures of Cu_5Sn_4 and SnO_2 are inserted into Nb1Zr tubes. We show that this design provides a flexible alternative artificial pinning centre (APC) vehicle for nano-precipitation of ZrO_2 in the A15 layer.

2. Methods

2.1 Wire Fabrication

Cu_5Sn_4 (η phase) was used as the Sn powder source rather than the $NbSn_2$ powder of the conventional ECN PIT design [23] because it is less costly and easier to make [24] (the Nb in the $NbSn_2$ does not contribute to the small-grain A15 phase, whereas the Cu in the Cu_5Sn_4 is required for the low temperature formation of Nb_3Sn). The Cu_5Sn_4 is made by mixing Sn and Cu powders with a starting composition of 59.9 wt.% Sn (an atomic ratio of Cu_5Sn_4 [25] and heat-treating them below 400 °C. A significant difference between $NbSn_2$-based PIT designs and this approach is that the η phase melts at 415 °C, well below the heat treatment temperatures used for Nb_3Sn formation. The Cu_5Sn_4 intermetallic is ball milled and then jet milled to a particle size that was typically 99% <3 μm (top size of 6 μm), so that the maximum particle size is significantly smaller than the ultimate filament core size to maintain composite stability during wire drawing. SnO_2 powder mixed with the Cu_5Sn_4 supplies the oxygen. For the composites supplied to BNL, two ratios of SnO_2:Cu_5Sn_4 were used, denoted "H" and "S", with the SnO_2 content in mixture "H" almost double that in "S". Wires with undisclosed SnO_2:Cu_5Sn_4 ratios were supplied to FSU and are described as compositions "$SnO_2$2X", "$SnO_2$1X" and "10SnO_2" to distinguish them from the BNL billet compositions. The mixed powder was packed into Cu-clad Nb-1wt%Zr tubes, which were then drawn to a restack size. Two multifilamentary composite designs were fabricated from these monocores; a 7-filament hexagonal stack (figure 1a) and a 120 filament octagonal assembly (figure 1b that was largely studied at BNL) that allows for the introduction of interfilamentary strengthening

Table I. Summary of PIT wires tested at BNL with Heat Treatment (HT) conditions

BNL Run	HT Temp, °C	HT Time, h	Cu/Non-Cu Ratio	Filaments	Filament Diameter, μm	Billet ID	SnO_2:Cu_5Sn_4 and Comments	Wire Dia., mm
3991	625	300	1.0	120	59	APC 550	SnO_2("S")	0.91
3993	650	200	1.0	120	59	APC 550	SnO_2("S")	0.91
3994	650	200	1.0	120	59	APC 550	SnO_2("S")	0.91
4051	632	200	1.0	120	51	APC 555	500 °C/24h+HT, SnO_2("H")	0.79
4133	630	100	1.0	120	59	APC 555	SnO_2("H")	0.91

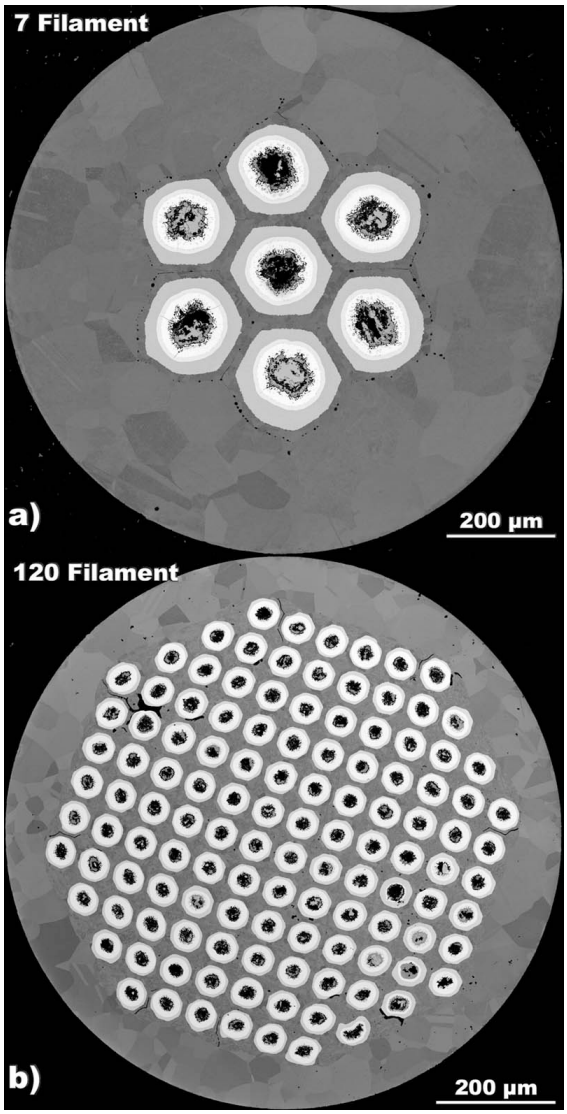

Figure 1. FESEM-BSE images of a) the reacted 7-filament (300 h/625 °C) and reacted 120 filament (200 h/640 °C) PIT composites.

elements [24]. The assembled multifilamentary composites were drawn to final diameters ranging from 1 to 0.5 mm. The strands supplied to BNL are summarized in table I.

2.2 Metallography

Short lengths of heat treated wires were provided by SupraMagnetics for microstructural and microchemical evaluation. The samples were polished in transverse cross-section and imaged using a Zeiss 1540EsB CrossBeam Field Emission Scanning Electron Microscope (FESEM). Microchemical analysis was performed in the FESEM using an EDAX Apollo XP SDD detector energy dispersive x-ray detector.

2.3 Magnetization Measurements

Magnetization measurements were performed on the short samples (~5 mm) using a 14 T Oxford Instruments dedicated Vibrating Sample Magnetometer (VSM) capable of operation at variable temperatures from 2 K to above T_c. The critical current density was estimated by the Bean model and the pinning force and Kramer curves were analyzed similarly to the transport data (see ahead).

2.4 Transport Measurements

Unreacted 120 filament wires were supplied to BNL for barrel heat treatment (HT) and measurement at magnetic fields up to 15 T. The ramp up to the HT reaction temperature was typically at a rate of 25 °C/h. Transport measurement was on a standard ITER with the central 7 turns in a uniform field, using the 0.1 µV/cm criterion and a measured sample length of 0.7 m. The data were analyzed by fitting the volume flux-pinning curve $F_p(H)$ (with self-field correction) to the generic expression $F_p(H)=C\cdot h^p(1-h)^q$, where C is a constant, $h=H/H_{irr}$, and H_{irr} is the irreversibility field. Standard process Nb_3Sn conductors without point pins are generally fit well by $p=0.5$ and $q=2.0$, which is essentially the Kramer fit [26] with B_{c2} being appropriately replaced by the Kramer field H_K extrapolation from ~10 to 15 T to define the irreversibility field at which J_c becomes zero.

3. Results

3.1. Microstructures

3.1.1. General Observations. The multifilament wires were difficult to draw to final size without breakage and even unbroken wires had broken filaments. In figure 2a we show five cross-sections from the same ~50 mm length of a 120 filament composite after a reaction heat treatment of 200 h

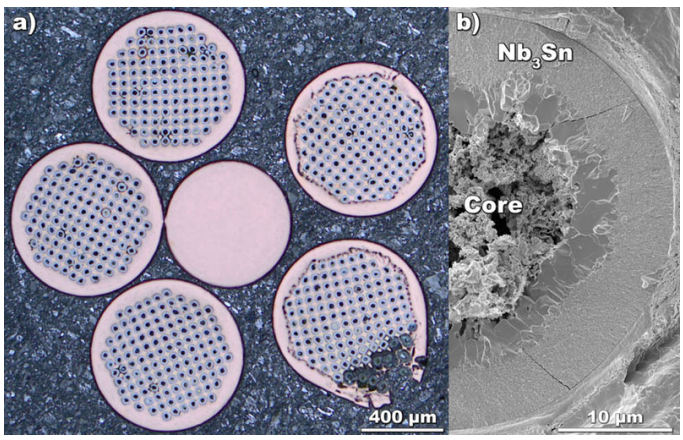

Figure 2. a) Light microscope image of five transverse cross sections from a 0.7 mm diameter 120 filament Nb1Zr+SnO_2 sample after a 200 h/650 °C heat treatment. These cross-sections showing Sn leakage and Sn burst are typical of the drawing issues experienced with these strands. b). FESEM-in-lens secondary electron image of a good filament from the same strand fractured to show the grain size. The small-grain Nb_3Sn layer is labelled.

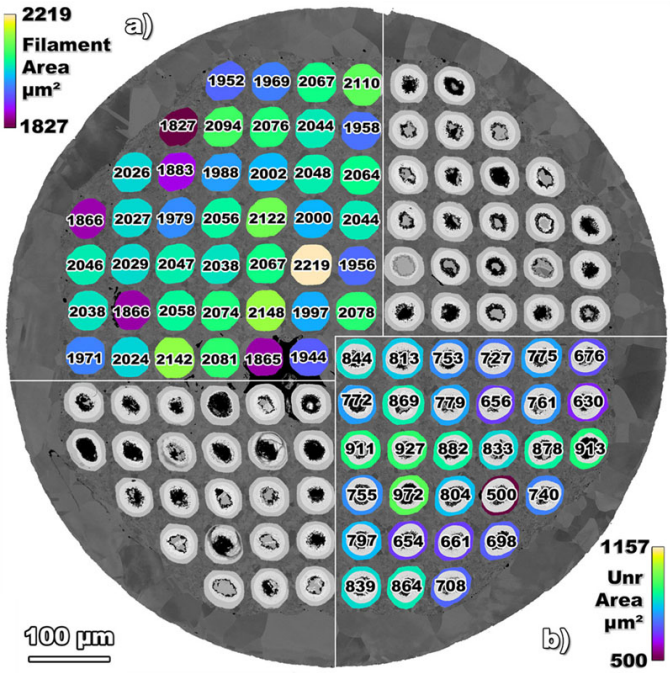

Figure 3. FESEM-BSE image of a 120 filament Nb1Zr+10SnO_2 sample after a 24h/500°C + 200h/650°C two-step heat treatment overlaid with quantitative analyses of the filament cross-sections. The top left quadrant analysis (a) indicates total area measurements of the filaments, whereas the bottom right quadrant analysis (b) indicates the residual Nb1Zr filament tube areas after the A15 reaction. The significant variation of un-reacted tube-cross-sectional areas is an indicator of pre-existing tube non-uniformities after drawing and prior to reaction.

at 650°C. A significant number of filament tubes have been breached and in one case there was Sn burst to the outside. Nevertheless, as shown in figure 2b, an extensive small-grain Nb_3Sn layer was found after reaction in the unbreached filaments of this strand.

The difficulty in drawing the composites to final size was attributed to a difficulty in obtaining Nb1Zr tube of the correct size and quality. Figure 3, is a cross-sectional BSE image of a 120 filament Nb1Zr+SnO_2 sample after a 24h/500°C + 200h/650°C two-step heat treatment that we have color-coded to contrast the total filament areas with the residual Nb1Zr areas after the A15 reaction. The quantitative image analysis indicated that the overall filament cross-sectional areas (as indicated in figure 3a) were fairly uniform, between 1800-2200 µm^2. The residual un-reacted Nb1Zr areas were much more variable, with the un-reacted areas differing by almost a factor of 2 from 500 µm^2 to 1100 µm^2. This large disparity is one indication of non-uniform deformation, and thinning of the Nb1Zr tubes during drawing as well as local variation induced by Sn loss from locally thinned and broken tube walls.

The samples were fractured to reveal the grain size as Nb_3Sn typically fractures along the grain boundaries. On these grain boundary fracture surfaces, we observed precipitate-like features similar in size and distribution to those observed by Xu *et al.* using TEM [27]. These features, assumed to be ZrO_2 precipitates, ranged in size from 5-15 nm in diameter but they were too small to confirm as ZrO_2 by compositional analysis in the FESEM. The oxidation of Zr is thermodynamically favoured over Nb, Sn and Cu and Rumaner *et al*. found by electron diffraction in TEM that the

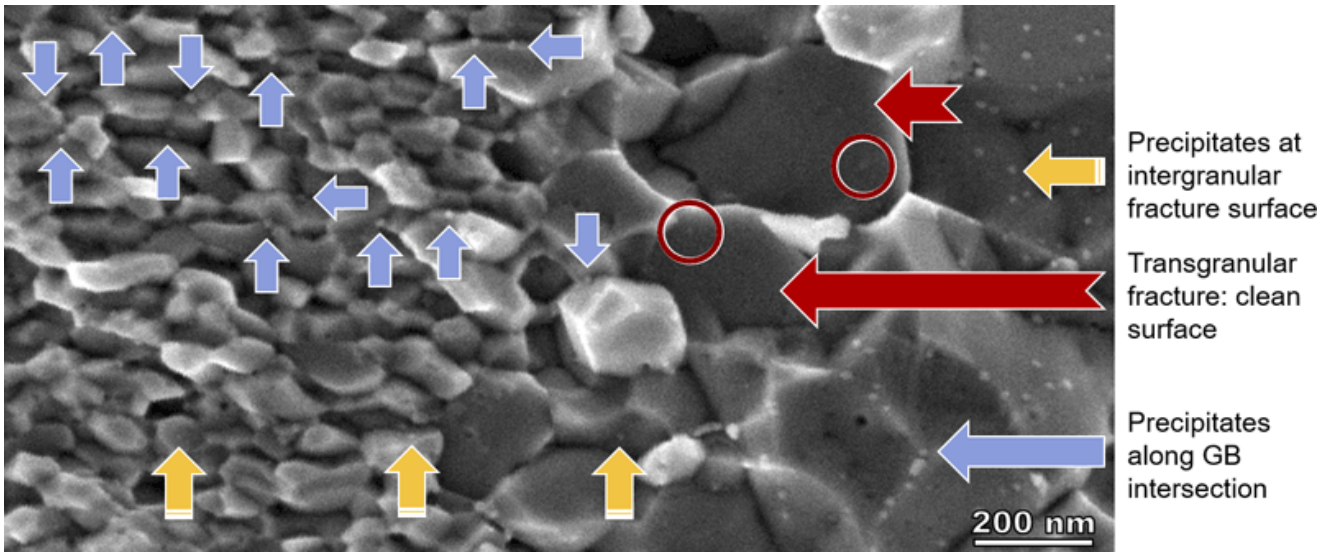

Figure 4. FESEM-in-lens secondary electron image of fracture surface at the interface between the large and small-grain regions in a representative region of a 120 filament Nb1Zr+"10SnO_2" sample after a 300h/630°C heat treatment. Precipitate-like features that we assume to be ZrO_2 are most commonly observed at grain boundary intersections (blue arrows) and less commonly at intergranular surfaces (orange arrows). For fractures through the grains (red arrows) there were no surface features but occasionally faint precipitate-scale contrast (red circles) that might indicate fracture through interior precipitates.

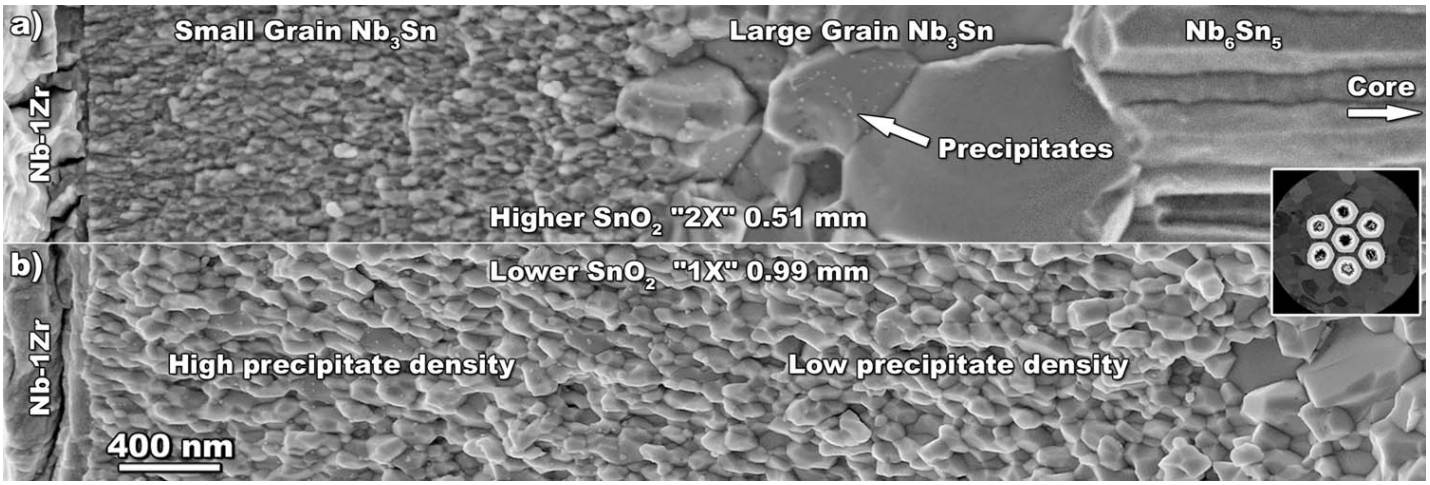

Figure 5. FESEM-in-lens secondary electron images of fracture surfaces of the small-grain Nb_3Sn layers in two 7-filament (inset) composites with different Cu_5Sn_4:SnO_2 ratios. Both samples were heat treated at 625 °C for 300 h, a) is at a wire diameter of 0.51 mm with higher ratio "$SnO_2$2X" and b) at 0.99 mm diameter with lower ratio "$SnO_2$1X". The higher SnO_2:Cu_5Sn_4 ratio produced an A15 grain diameter that was ~ half the lower ratio "$SnO_2$1X" sample. We did not observe precipitate contrast in the transgranular fractures.

precipitates in their Nb-1Zr experiments (by a quite different approach and using high temperatures where the Zr is more mobile) were monoclinic ZrO_2 [20]. We did not observe particles in fractured surfaces in a Ta-doped PIT sample using the same Cu_5Sn_4 powder but no SnO2 or Zr [25], however, fracture performed elsewhere of Nb_3Sn that was not designed for oxidation has produced surface particulates of similar size and contrast [28,29]. An example of the precipitates at the interface between the large and small grain A15 regions is shown in figure 4. The precipitates are sparsely distributed with rarely more than one precipitate per grain boundary segment in the small-grain regions. Most commonly, the precipitates are observed at grain boundary intersections (some examples are indicated by the blue arrows in figure 4). Less frequently, the precipitates are observed at grain boundary surfaces (as indicated by the orange arrows in figure 4). In figure 4 we also show some large grains (red notched arrows) that have fractured through the grains rather than at the grain boundaries, and in these we see no surface precipitates. There is, however, some faint contrast on the scale of the ZrO_2 precipitates that might suggest that the fracture has sliced through precipitates.

3.1.2 Cu_5Sn_4:SnO_2 ratio

In figure 5 fracture surfaces from two 7-filament composites with different Cu_5Sn_4:SnO_2 ratios but the same heat treatment (300h/625°C) are contrasted. Composition "$SnO_2$2X" (figure 5a), is higher in SnO_2 and produces a much finer (<30 nm diameter near the Nb1Zr interface) A15 grain size than composition "$SnO_2$1X" (figure 5b). However, there is a clear grain size gradient with the grain diameter becoming smaller towards the Nb1Zr interface (outer edge of reaction front). However, the small grain layer is ~ half the thickness for lower SnO_2 "$SnO_2$1X" strand. This might be related to the smaller strand diameter (0.51 mm compared with 0.91 mm) or that the reaction is proceeding slower. The precipitates also appear to be smaller for the higher SnO_2 ratio sample. All the samples had an interior layer of much larger A15 grains, as is found for conventional PIT Nb_3Sn wire. As indicated in figure 5b, closer to the core in the low-SnO_2 sample, the precipitate density is greatly reduced, suggesting a depleted oxygen supply in the low SnO_2 sample and inability to convert all the Zr to ZrO_2. The area-equivalent A15 grain diameter for the low-SnO_2 sample increased from ~77 nm at the Nb-1Zr interface to ~86 nm at the small-grain:large-grain interface. Both samples have a thick Nb_6Sn_5 layer adjacent to the large-grain Nb_3Sn layer. This thick interior layer of Nb_6Sn_5 is effectively a trapped Sn supply because bulk diffusion of Sn through Nb_3Sn is orders of magnitude slower than along grain boundaries [30] and the large grains offer sparse outward diffusion paths for the Sn. Note that, unlike conventional PIT Nb_3Sn which uses $NbSn_2$ powder in the core as the Sn source, in this SupraMagnetics Cu_5Sn_4 core design all the Nb for the Nb_3Sn and Nb_6Sn_5 phases is supplied by the Nb1Zr tube.

In these 7-filament composites the small-grain Nb_3Sn area was only 7.1% of the filament cross-section for the sample in figure 5a and 9.9% for the sample in figure 5b compared with ~40% of the cross-section for fully optimized accelerator quality PIT Nb_3Sn strands [11,31].

3.1.3 Microstructural Gradients The A15 grain size gradient in figure 5a is quantified in figure 6 in terms of area equivalent grain diameter (the diameter calculated from the

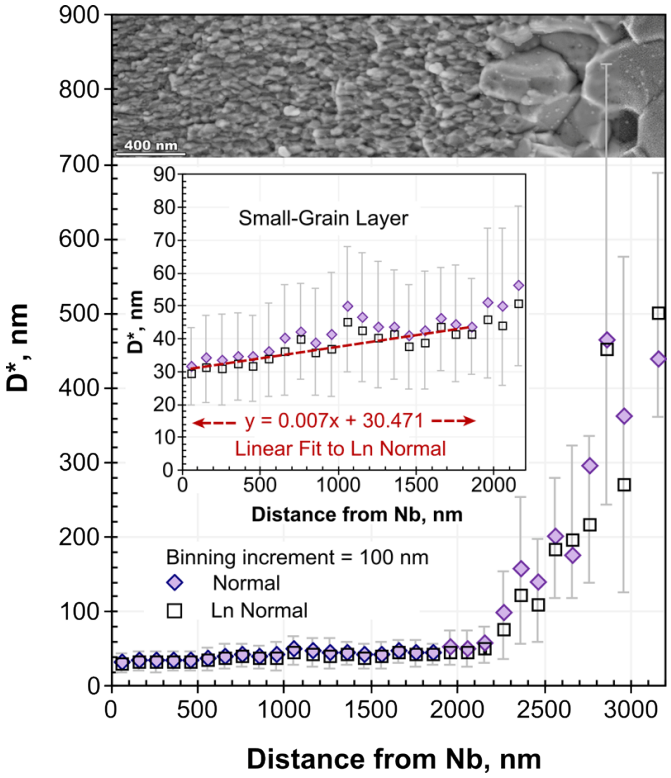

Figure 6. Area equivalent grain diameter variation with distance from the unreacted Nb1Zr interface for the high SnO_2:Cu_5Sn_4 composition "$SnO_2$2X" 7-filament strand in figure 5a. The size distribution is log-normal but both log-normal and normal averages for each bin are applied for comparison with other published data. The least-squares linear fit is applied to the log-normal data across the small grain range indicated. Error bars show ± one sample standard deviation based on log-normal statistics for each bin.

cross-section area assuming a circular cross-section). The A15 grain diameter is as small as 30 nm near the unreacted Nb1Zr interface and rises to a little over 40 nm near the original growth front neighbouring the large-grain region. The error bars show the log-normal standard deviations. Both values are much smaller than the ~90-150 nm size in conventional Zr-free A15 wires.

The impact on vortex pinning should be clearer when plotted in terms of grain boundary density, as is shown in figure 7, which increases by about 40% towards the outer edge of the reaction front. Because the grain size of the last A15 to form is smaller than that at the original core/Nb1Zr interface, it appears that some grain growth occurs as the A15 reaction front penetrates into the tube.

In figure 8 we plot the Nb_3Sn grain aspect ratio against distance from the Nb1Zr tube interface. We find a very constant aspect ratio across the fine grain region. A low Sn content as occurs at the Nb-A15 interface is often associated with an increase in A15 grain aspect ratio so this result is

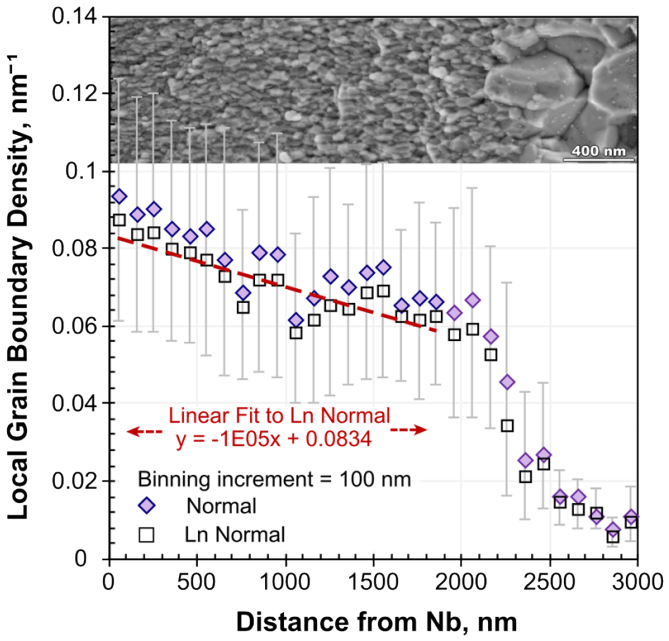

Figure 7. Decrease of Nb_3Sn grain boundary density with increasing distance from the reaction front at the Nb1Zr interface for the high SnO_2:Cu_5Sn_4 composition "$SnO_2$2X" 7-filament strand in figure 5a. The size distribution is log-normal but the mean of both log-normal and normal for each bin are presented. The least-squares fit is applied to the log-normal data across the small grain size range indicated. Error bars show ± one sample standard deviation based on log-normal statistics for each bin.

consistent with the uniform compositions reported in figure 9a and b. The ZrO_2 precipitates may, however, also play a

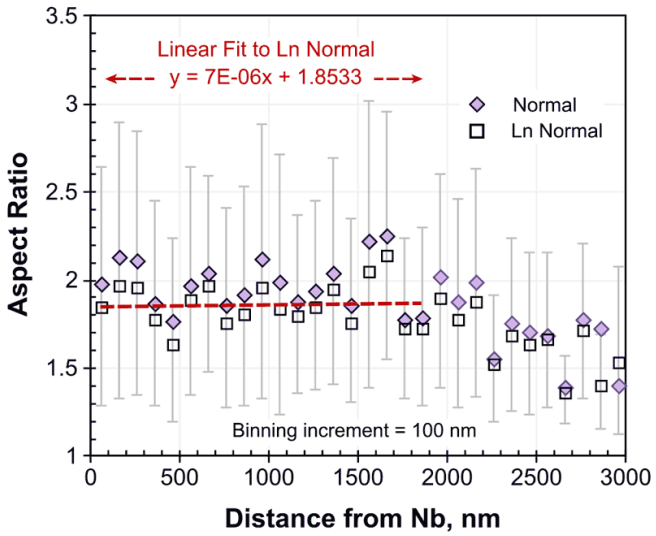

Figure 8. The aspect ratios for the Nb_3Sn grains as a function of distance from the unreacted Nb1Zr interface for the high SnO_2:Cu_5Sn_4 composition "$SnO_2$2X" 7-filament strand in figure 5a. The least-squares fit indicates that the aspect ratio is remarkably uniform across the small-grain A15 layer. The least-squares fit is applied to the log-normal data across the small grain range indicated. Error bars show ± one sample standard deviation based on log-normal statistics for each bin.

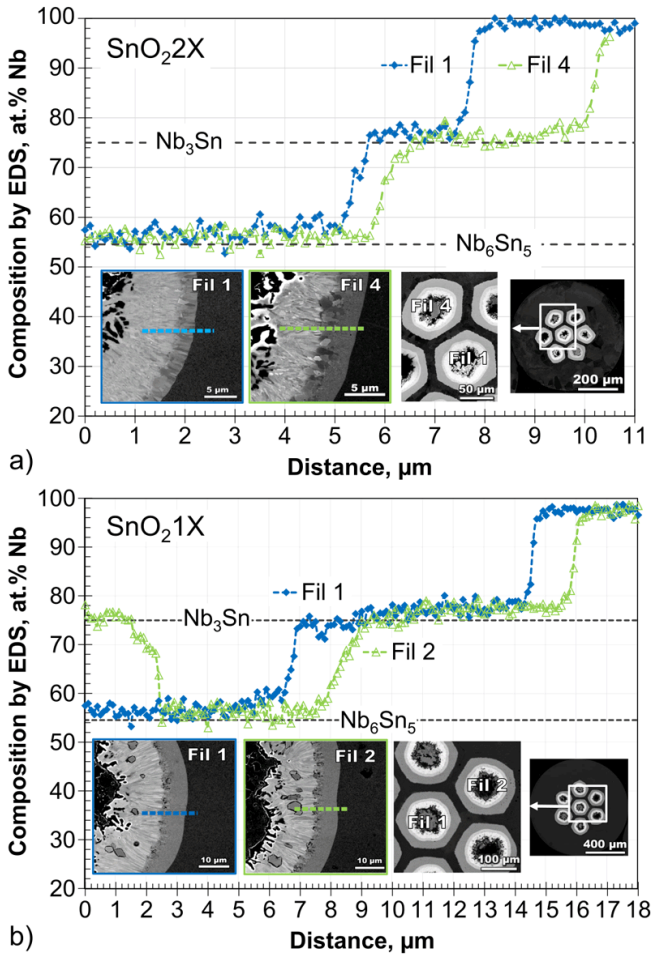

Figure 9. EDS analysis of 7-filament Zr/SnO_2 with a) Cu_5Sn_4:SnO_2 ratio "$SnO_2$2X" (strand in figure 5a) and b) "$SnO_2$1X" (strand in figure 5b), both heat treated for 300 h/625 °C. In a) the thicker "Fil 4" Nb_3Sn layer has a composition that is closer to stoichiometry than the central "Fil 1", suggesting some Sn loss from this filament. In b) the Nb_6Sn_5 layer contains some large Nb_3Sn grains 1-3 μm in diameter

role in nucleating new A15 grains and in this way inhibit columnar growth.

3.1.4 Microchemical analysis. EDS analyses of filaments layers from the $SnO_2$2X, and $SnO_2$1X samples shown in figure 5 are shown in figure 9a and 9b respectively. The composition of Nb_3Sn produced during the final reaction heat treatment is close to stoichiometric across most of the Nb_3Sn layer for Filament 4 in figure 9a ($SnO_2$2X) but is Sn-poor for the thinner A15 layer in the central filament (Filament 1) suggesting that there has been Sn loss through the tube to the surrounding Cu in this filament. The Sn composition for Filament 4 of the $SnO_2$2X wire eventually declines over the outer ~1 μm of the small-grain layer.

For the $SnO_2$1X sample, both filaments shown in figure 9b have a composition gradient across the A15 layer. An

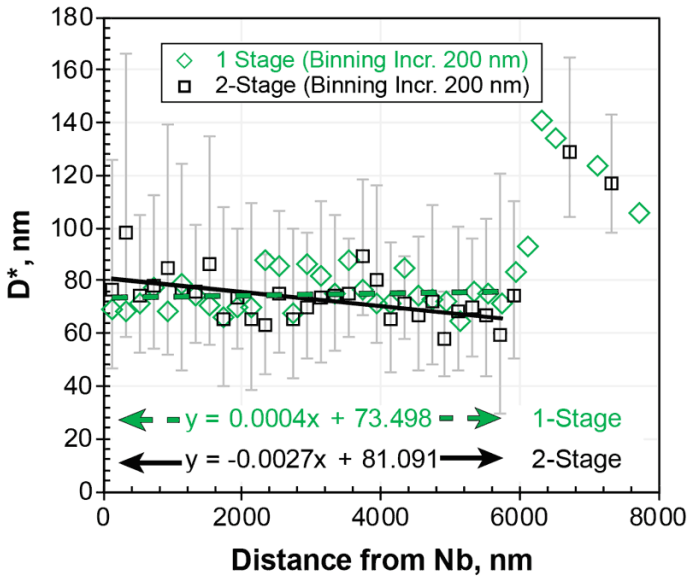

Figure 10. Area equivalent grain diameter (ln-normal) variation with distance from the unreacted Nb-1Zr interface for a 120 filament Nb1Zr+10SnO_2 composite heat treated with a single 300 h/630 °C heat treatment (green) and a dual stage HT of 200 h/625 °C + 100 h/650 °C (black). The grain size is similar at the center of the layer (< 80 nm) but the 2-stage heat treatment produces an A15 grain size gradient across the layer). Least-square linear fits are shown for the data across the small grain layers.

interesting observation is that there are large Nb_3Sn grains that occur deep inside the Nb_6Sn_5 layer in filaments with the lower SnO_2 composition "$SnO_2$1X" wire, as is seen in figure 9b. For conventional PIT made with $NbSn_2$ powder precursor, Nb_6Sn_5 is an intermediate reaction phase that forms adjacent to the Nb tube during A15 layer growth and invariably decomposes to large-grain A15 by loss of Sn to the growing small-grain Nb_3Sn layer. The fact that a residual Nb_6Sn_5 layer is found at the interface indicates imperfect Sn diffusion into the filament tube that could have enabled further small-grain A15 layer growth.

3.1.5 Two-Stage Reaction Heat Treatment. In figure 10 we compare the Nb_3Sn area-equivalent grain diameters of the same 120 filament Nb1Zr+10SnO_2 composite heat treated with a single HT of 300 h at 630 °C with a dual stage HT (200 h/625 °C + 100 h/650 °C) starting at a lower and finishing at a higher temperature. The dual-stage heat treatment with a final stage at 650 °C did not greatly coarsen the grain size as compared to the single HT (the average grain size of < 80 nm for both strands is small for PIT Nb_3Sn) as is usually the case for Zr-free wires. The rationale for the second, higher temperature 650 °C step is to drive more compositional uniformity across the A15 layer assuming that it is possible to establish a fine grain size at the lower temperature of the first stage. It seems that this has been quite successful because the initially formed grains furthest away from the unreacted Nb1Zr interface are small (~70 nm)

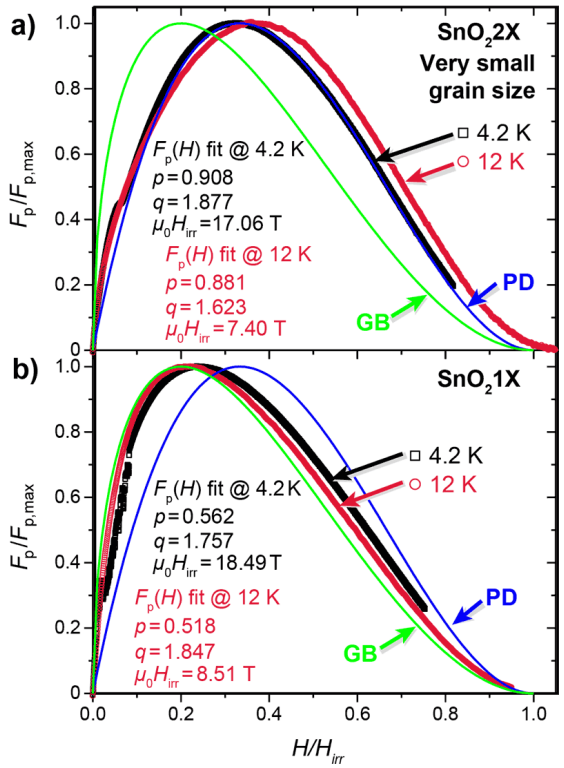

Figure 11. Normalized pinning force curves for a) composition "$SnO_2$2X" with small grains and b) composition "$SnO_2$1X" with larger grains at 4.2 K and 12 K. The ideal curves for grain boundary GB (green) and point defect PD (blue) pinning are also shown and the fitting parameters are reported.

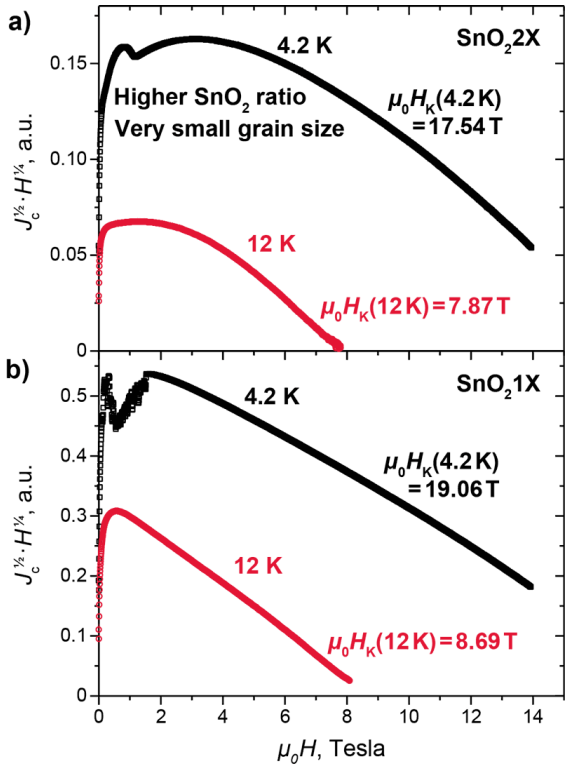

Figure 12. A comparison of the magnetization-derived Kramer plots for a) the high SnO_2:Cu_5Sn_4 composition "$SnO_2$2X" wire with smaller grains and b) composition "$SnO_2$1X" wire with larger grains and less ZrO_2 at 4.2 K and 12 K. The very small grain size microstructure (a) shows a clear deviation from the usual linearity of Kramer plots for Zr-free Nb_3Sn wires.

and the final grains only slightly larger (~80 nm). This compares with a d* of ~90 nm for a similarly heat treated (280 h/625 °C) Nb-Ta, Zr-free. PIT strand [11].

3.2 Magnetization results

Magnetization measurements at FSU enabled both 4.2 and 12 K properties to be obtained with derivation of the whole F_P curve at 4.2 and 12 K (shown in figure 11) for the samples whose microstructures are shown in figure 5. Higher SnO_2:Cu_5Sn_4 ratio "$SnO_2$2X" produced a very small Nb_3Sn grain size of ~30-40 nm, and pinning force curves peaking at higher reduced field with a curve shape approaching that expected for point defect (PD) pinning. In contrast, composition "$SnO_2$1X" produced a curve peaking at lower reduced field that more closely matched that for sparse grain boundary (GB) pinning, consistent with its larger grain size. If the precipitates in the "$SnO_2$2X" sample are also smaller they may be more effective as point pinning sites. However, fitting the pinning force curves with the generic relation $F_p/F_{p,max} \propto (H/H_{Irr})^p(1 - H/H_{Irr})^q$, $\mu_0 H_{irr}$(4.2 K) for composition "$SnO_2$2X" fell to 17.1 T compared with 18.5 T for composition "$SnO_2$1X". Both values are smaller than would be expected from binary Zr-free wires. Also the p and q parameters are close to the values for GB pinning for "$SnO_2$1X" and close to the values for PD pinning for "$SnO_2$2X".

Alternatively, using a two-contribution fit (see section 3.3), the relative contributions of PD and GB pinning were 89% PD, for composition "$SnO_2$2X", but only 24% for "$SnO_2$1X", consistent with the smaller precipitate density of the lower SnO_2:Cu_5Sn_4 core wire. The estimated small-grain-layer $J_{cm\text{-}layer}$(4.2 K, 12 T) for the high SnO_2:Cu_5Sn_4 composition "$SnO_2$2X" was ~ 4500 A/mm^2 (a high value for a Zr-free strand compared to our previous highest small-grain layer 12 T J_c value for a binary conventional PIT strand of 3300 A/mm^2 [32]). For composition "$SnO_2$1X" the estimated small-grain-layer $J_{cm\text{-}layer}$(4.2 K, 12 T) was about 2900 A/mm^2, thus showing no advantage.

In figure 12 we compare the magnetization-derived Kramer plots for the same samples as in figure 11. The Kramer plot should be linear if sparse grain boundaries are the only effective pinning centres. However, we do observe a distinctly non-linear Kramer plot in the ultra-small grain sized sample (composition "$SnO_2$2X"), which also had a markedly higher layer J_c.

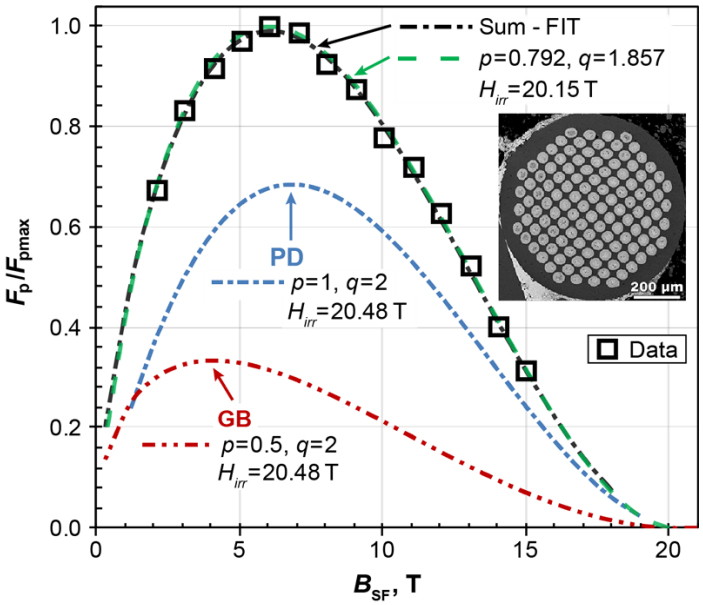

Figure 13. The normalized F_p is plotted as a function of the reduced field for Run # 3991: SnO_2("S")+Nb1Zr 300h@625°C: 120 Filament APC. The deconvolution into GB and PD pinning components shows that PD pinning dominates with 68% contribution to F_p. H_{irr} is found to be 20.48 T. When the exponents and H_{irr} are allowed to vary, the best fit to the data is shown by the dashed curve, which is very close to the summation curve.

3.3 Transport measurements

Billets L550 and L555 used the 120 filament PIT design with lower and higher SnO_2 ratios respectively. Consistent with the cross-sections, evidence of damage to the filaments appeared in the degraded *n*-values of ~ 5. However, even though the transport critical currents are low due to poor filament quality, it was possible to measure their I_c from 15 T to very low fields, and thus determine the normalized flux-pinning curve, $f_p=F_p/F_{p\,max}$, as a function of field. Measurements below 2 T are not shown, since they then include an additional contribution from the un-reacted Nb.

The I_c measurements were fitted by varying the parameters p and q and B_{c2}. An example is shown in figure 13 where the normalized F_p is plotted as a function of the self-field corrected magnetic field, B_{SF}, for a strand from billet 550 reacted at 625 °C for 300 h. The best overall fit is obtained for p=0.792, q=1.857 and B_{c2}=20.15 T. The non-standard exponents p and q suggest that the pinning is not only from grain-boundary pinning (p=0.5, q=2.0), but also from an additional contribution, as has been observed in enhanced J_c Nb_3Sn wires with radiation-induced point defects within the grains [33]. These additional point pins shift the maximum of the pinning curve from b = 0.20 to b ~ 0.27. Indeed, we can realistically deconvolute the data set of figure 13 into two components with fixed classical p and q values of $p = 1$, $q = 2$ for point defect pinning (PD) and $p = 0.5$, $q = 2$ for grain boundary (GB) pinning, where the point defect component dominates the total pinning, especially at higher fields where higher J_c is most desirable .

The analyses of the transport-current-tested strands are summarized in table II. The best pinning force fits were found for two-component PD + GB pinning for all the APC strands. The PD contribution ranged from 65% to 76%. Billet 555 had a higher proportion of SnO_2 powder in the core but had similar PD contributions to the other billet. In fact the lowest PD value was obtained from billet 555 strand that was reacted with a slow ramp rate of 10 °C/h from room temperature to 630 °C and held there for 100 h to reduce grain growth and thereby increase the GB pinning density. It appears that increasing the SnO_2 powder fraction in this composite does little to enhance the pinning, although the B_{c2} is ~ 2 T higher than that observed for billet 550.

4. Discussion

Despite the poor filament quality arising from low quality Nb1Zr tubes, the results reported here show that the PIT approach with Cu_5Sn_4 and SnO_2 is a viable method to deliver oxygen for the internal oxidation of Zr in Nb. By incorporating Cu as η-Cu_5Sn_4 in the powder core, the Cu can reduce the reaction temperature without blocking oxygen

Table II. Summary of J_c and *n*-values (12 T, 4.22 K, non-self-field corrected) and Pinning Force fits for PIT wires tested at BNL

Run No	Billet	HT	J_c (non-Cu A/mm²)	*n*	*p*	*q*	*C*†	H_{irr} (T)	Two component fit:	H_{irr} (T)	% PD
3991	550	300h/625°C	109	3.3	0.79	1.86	9.44	20.15	PD (p=1) and GB (p=0.5)	20.48	68%
3993	550	200h/650°C	162	3.5	0.72	1.42	10.09	18.82	PD (p=1) and GB (p=0.5)	21.08	69%
3994	550	200h/650°C	182	3.9	0.80	1.67	13.11	19.74	PD (p=1) and GB (p=0.5)	20.80	76%
4051	555‡	48h/540°C, 200h/632 °C	89	2.6	0.78	1.66	5.14	21.79	PD (p=1) and GB (p=0.5)	23.30	71%
4133	555‡	10°C /h + 100h/630°C	42	2.6	0.75	1.65	3.06	21.40	PD (p=1) and GB (p=0.5)	22.79	65%

† = slope of the Kramer plot of F_p (A·T/mm²) vs. $b^p\cdot(1\text{-}b)^q$ ‡ = higher proportion of SnO_2 powder in the core

diffusion as was the case with earlier attempts at internal oxidation [21]. Recent work by Xu *et al*. [34] has indicated that Nb-Sn intermetallics may still impede oxygen diffusion from the core requiring more SnO_2 and further HT modification to overcome this issue.

Both magnetization and transport measurements on the SupraMagnetics strands showed that this approach of introducing ZrO_2 precipitates and refining the grain size from 90 nm in Zr-free wires to less than 40 nm shifts the peak in the pinning force curve from about b ~0.2 to as high as 0.35 in figure 11, as is expected from a large point pinning component. These results are similar to the very small grain size (20-50 nm diameter) films [35] that produced a shift in the peak of $F_p(H)$ to almost $0.4H_{irr}$ in thin films (Nb sputtered onto a bronze substrate and then reacted). Using transport J_c barrel measurements, the F_p curves could be deconvoluted into a dominant PD contribution (65%) to F_p that is similar to the point defect irradiation effects observed by Baumgartner *et al.*[33]. An even larger 89% PD contribution was estimated by magnetic measurements on the 30-45 nm grain size sample.

For high field magnet conductor use there is still some uncertainty as to the potential of this approach as there was significant suppression of the Kramer extrapolated fields for all samples. Normally speaking the $\mu_0 H_{c2}$ of binary Nb_3Sn is 23-24 T [36], as compared to the ~17.5-22 T values found here (which are similar to the values of 20.5 and 21.3 T obtained by Xu *et al* for their Nb1Zr APC [22]). The depression was notably larger for the higher SnO_2 7-filament sample with the very small A15 grain size. Whether the degradation of H_{irr} is due to Zr or perhaps to strain induced by ZrO_2 within the A15 grains is not yet clear but this is something that needs verification because a high critical field is essential for reaching high critical currents at fields above 16 T. All modern Nb_3Sn wire use Ta or Ti or a combination of Nb and Ti dopants to increase their high-field performance by increasing H_{c2} [37] and verification of the effectiveness of ZrO_2 using Nb alloys containing Ti or Ta to enhance the upper critical field will be needed.

5. Conclusions

1. A viable route to an APC (artificial pinning centre) Nb_3Sn has been demonstrated in multifilamentary PIT strand by internal oxidation of Nb1Zr tubes using a core powder mixture of η-phase Cu_5Sn_4 powder and SnO_2. However, the volume of small-grain Nb_3Sn produced in these demonstration samples was only ~18-25% of that for modern accelerator-quality PIT Nb_3Sn, so significant improvements in package efficiency and heat treatment optimization will be required to make this process competitive.

2. Cu_5Sn_4 does not appear to interfere with the diffusion of oxygen from SnO_2/ Cu_5Sn_4 powder mixtures into Nb1Zr filament tubes. This suggests that only small modifications to existing internal Sn and PIT approaches will be necessary to fully prove out this method of enhancing vortex pinning in Nb_3Sn, providing that pure Cu does not sit between the Sn and Nb1Zr during the reaction step.

3. A shift in the peak of the pinning force curve to higher reduced fields was similar to that observed for APC thin films and recent radiation experiments. However, as in recent work by Xu *et al*.[22], the Kramer fields were significantly depressed from that found in the best Zr-free binary conductors.

4. The pinning force curves can be deconvoluted into contributions from point and grain boundary pinning with point pinning supplying up to 89% of the pinning force for the APC strands in the most favourable case. The estimated Nb_3Sn small-grain layer J_{cm} (12 T, 4.2 K) was ~36% higher than that previously reported for a conventionally processed binary PIT.

5. The applicability of this technique to optimizing high field performance still needs to be demonstrated using alloys incorporating Ti and/or Ta to increase H_{c2}.

6. Better tube quality that maintains its integrity through the drawing cycle so that η phase is not lost when melted and an understanding of why some filaments are left with partial Nb_3Sn reactions and thick Nb_6Sn_5 layers should yield much better critical current values. The issue of microstructural gradients will also have to be addressed.

Acknowledgments

This material is based upon work supported by the U.S. Department of Energy, Office of Science, Office of High Energy Physics under SBIR Program award DE-SC0009605 with additional support from award DE-SC0012083 and the State of Florida. The NHMFL is supported by the NSF under award NSF-DMR-1157490. Jeremiah McCallister provided additional metallographic support.

References

[1] Devred A, Backbier I, Bessette D, Bevillard G, Gardner M, Jong C, Lillaz F, Mitchell N, Romano G and Vostner A

2014 Challenges and status of ITER conductor production *Superconductor Science and Technology* **27** 044001

[2] Bottura L, de Rijk G, Rossi L and Todesco E 2012 Advanced Accelerator Magnets for Upgrading the LHC *IEEE Transactions on Applied Superconductivity* **22** 4002008–4002008

[3] Ambrosio G 2015 Nb_3Sn High Field Magnets for the High Luminosity LHC Upgrade Project *IEEE Transactions on Applied Superconductivity* **25** 1–7

[4] Jiang J, Francis A, Alicea R, Matras M, Kametani F, Trociewitz U P, Hellstrom E E and Larbalestier D C 2017 Effects of Filament Size on Critical Current Density in Overpressure Processed Bi-2212 Round Wire *IEEE Transactions on Applied Superconductivity* **27** 1–4

[5] Rossi L, 2016 High-Luminosity LHC *Proceedings of the International School of Physics "Enrico Fermi"* **194** (Future Research Infrastructures: Challenges and Opportunities) 61–72

[6] Tommasini D, Auchmann B, Bajas H, Bajko M, Ballarino A, Bellomo G, Benedikt M, Bermudez S I, Bordini B, Bottura L, Buzio M, Dhalle M, Durante M, de Rijk G, Fabbricatore P, Farinon S, Ferracin P, Gao P, Lackner F, Lorin C, Marinozzi V, Martinez T, Munilla J, Ogitsu T, Ortwein R, Perez J, Prioli M, Rifflet J-M, Rochepault E, Russenschuck S, Salmi T, Savary F, Schoerling D, Segreti M, Senatore C, Sorbi M, Stenvall A, Todesco E, Toral F, Verweij A P, Volpini G, Wessel S and Wolf F 2017 The 16 T Dipole Development Program for FCC *IEEE Transactions on Applied Superconductivity* **27** 1–5

[7] Schoerling D, Durante M, Lorin C, Martinez T, Ruuskanen J, Salmi T, Sorbi M, Tommasini D and Toral F 2017 Considerations on a Cost Model for High-Field Dipole Arc Magnets for FCC *IEEE Transactions on Applied Superconductivity* **27** 1–5

[8] Ballarino A and Bottura L 2015 Targets for R&D on Nb_3Sn conductor for High Energy Physics *IEEE Transactions on Applied Superconductivity* **25** 1–6

[9] Cooley L D, Ghosh A K, Dietderich D R and Pong I 2017 Conductor Specification and Validation for High-Luminosity LHC Quadrupole Magnets *IEEE Transactions on Applied Superconductivity* **27** 1–5

[10] Sanabria C, Lee P J and Larbalestier D C 2017 The vital role of a well-developed Sn-Nb-Cu membrane for high J_c RRP Nb_3Sn wires *unpublished result, presentation STP531 (4MOr2A-04).[Online]. Available: http://snf. ieeecsc. org/snf-issue-no-38-october-2016,*

[11] Tarantini C, Segal C, Sung Z H, Lee P J, Oberli L, Ballarino A, Bottura L and Larbalestier D C 2015 Composition and connectivity variability of the A15 phase in PIT Nb_3Sn wires *Superconductor Science and Technology* **28** 095001

[12] Scanlan R M, Fietz W A and Koch E F 1975 Flux pinning centers in superconducting Nb_3Sn *Journal of Applied Physics* **46** 2244–9

[13] Gauss S and Flükiger R 1987 Powder metallurgical alternative for the processing of $(Nb\text{-}Ta)_3Sn$ multifilamentary wires, starting from elementary Nb and Ta powder *Magnetics, IEEE Transactions on* **23** 657–660

[14] De Moranville K, Yu D and Wong J 1993 Development of a niobium-tin multifilamentary wire with artificial tantalum inclusions *IEEE transactions on applied superconductivity* **3** 982–985

[15] Kitai T, Higuchi M and Osamura K 1997 Artificial pinning centres in jelly-roll processed NbCu composites *Cryogenics* **37** 389–395

[16] Rodrigues C A and Rodrigues D 2006 Development and characterization of Nb_3Sn superconductor wire with nanometric-scale pinning centers *Journal of Physics: Conference Series* **43** 43–6

[17] Dietderich D R and Scanlan R M 1995 Characterization of superconductors with artificial pinning microstructures *IEEE Transactions on Applied Superconductivity* **5** 1777–1780

[18] Dietderich D R and Scanlan R M 1997 Nb_3Sn artificial pinning microstructures *Applied Superconductivity, IEEE Transactions on* **7** 1201–4

[19] Dietderich D R, Kelman M, Litty J R and Scanlan R M 1998 High Critical Current Densities in Nb_3Sn Films with Engineered Microstructures — Artificial Pinning Microstructures *Adv. Cryo. Eng.* **44** 951–8

[20] Rumaner L E, Benz M G and Hall E L 1994 The role of oxygen and zirconium in the formation and growth of Nb_3Sn grains *Metallurgical and Materials Transactions A* **25** 213–219

[21] Zeitlin B A, Gregory E, Marte J, Benz M, Pyon T, Scanlan R and Dietderich D 2005 Results on Mono Element Internal Tin Nb_3Sn Conductors (MEIT) With Nb7.5Ta and Nb(1Zr + O_X) Filaments *IEEE Transactions on Applied Superconductivity* **15** 3393–8

[22] Xu X, Sumption M, Peng X and Collings E W 2014 Refinement of Nb_3Sn grain size by the generation of ZrO_2 precipitates in Nb_3Sn wires *Applied Physics Letters* **104** 082602

[23] Elen J, Van Beijnen C and Van der Klein C 1977 Multifilament V_3Ga and Nb_3Sn superconductors produced by the ECN-technique *IEEE Transactions on Magnetics* **13** 470–473

[24] Motowidlo L R and Ozeryansky G M 2008 A New PIT Nb_3Sn Conductor for High Magnetic Field Applications *IEEE Transactions on Applied Superconductivity* **18** 1001–4

[25] Motowidlo L R and Ozeryansky G M 2008 A Nb_3Sn Conductor via Cu_5Sn_4 PIT Process for High Field Applications *AIP Conference Proceedings* **986** 269–76

[26] Kramer E J 1973 Scaling laws for flux pinning in hard superconductors *Journal of Applied Physics* **44** 1360–70

[27] Xu X, Sumption M D and Peng X 2015 Internally Oxidized Nb_3Sn Strands with Fine Grain Size and High Critical Current Density *Advanced Materials* **27** 1346–50

[28] Bhartiya S, Sumption M D, Xuan Peng, Gregory E, Tomsic M J and Collings E W 2009 Investigation of the Effects of Low Temperature Heat Treatments on the Microstructure and Properties of Multifilamentary, Tube-Type Nb_3Sn Strands IEEE Transactions on Applied Superconductivity 19 2588–92

[29] X. Xu 2017 Fermilab, private communication.

[30] Farrell H H, Gilmer G H and Suenaga M 1974 Grain boundary diffusion and growth of intermetallic layers: Nb_3Sn *Journal of Applied Physics* **45** 4025–35

[31] Segal C, Tarantini C, Sung Z H, Lee P J, Sailer B, Thoener M, Schlenga K, Ballarino A, Bottura L, Bordini B, Scheuerlein C and Larbalestier D C 2016 Evaluation of critical current density and residual resistance ratio limits in powder in tube Nb_3Sn conductors *Superconductor Science and Technology* 29 085003

[32] Lee P J, Fischer C M, Naus M T, Squitieri A A and Larbalestier D C 2003 The microstructure and microchemistry of high critical current Nb_3Sn strands manufactured by the bronze, internal-Sn and PIT techniques *IEEE Transactions on Applied Superconductivity* **13** 3422–5

[33] Baumgartner T, Eisterer M, Weber H W, Flükiger R, Scheuerlein C and Bottura L 2015 Performance Boost in Industrial Multifilamentary Nb_3Sn Wires due to Radiation Induced Pinning Centers *Scientific Reports* **5 10236**

[34] Xu X, Peng X, Sumption M and Collings E W 2017 Recent Progress in Application of Internal Oxidation Technique in Nb_3Sn Strands *IEEE Transactions on Applied Superconductivity* **27** 1–5

[35] Cooley L D and Lee P J 2001 Shift of the flux-pinning force curve in Nb_3Sn thin films with very fine grain size *Applied Superconductivity, IEEE Transactions on* **11** 3820–3823

[36] Fischer C, Lee P and Larbalestier D 2002 Irreversibility Field and Critical Current Density as a Function of Heat Treatment Time and Temperature for a Pure Niobium Powder-In-Tube Nb_3Sn Conductor *Advances in cryogenic engineering* **48** 1008–1015

[37] Suenaga M, Welch D O, Sabatini R L, Kammerer O F and Okuda S 1986 Superconducting critical temperatures, critical magnetic fields, lattice parameters, and chemical compositions of ‘“bulk”’ pure and alloyed Nb_3Sn produced by the bronze process Journal of *Applied Physics* **59** 840